Detecting abnormal vasculature from photoacoustic signals using wavelet-packet features

Jason Zalev and Michael C. Kolios

Ryerson University, 350 Victoria Street, Toronto, Canada

ABSTRACT

Photoacoustic systems can produce high-resolution, high-contrast images of vascular structures. To reconstruct images at very high-resolution, signals must be collected from many transducer locations, which can be time consuming due to limitations in transducer array technology. A method is presented to quickly discriminate between normal and abnormal tissue based on the structural morphology of vasculature. To demonstrate that the approach may be useful for cancer detection, a special simulator that produces photoacoustic signals from 3D models of vascular tissue is developed. Results show that it is possible to differentiate tissue classes even when it is not possible to resolve individual blood vessels. Performance of the algorithm remains strong as the number of transducer locations decreases and in the presence of noise.

Keywords: Photoacoustic, optoacoustic, wavelet packet, tissue classification, vascular morphology

1. INTRODUCTION

1.1 Motivation

It is well known to cancer researchers that normal vascular tissue has a highly organized branching structure, while cancerous tissue usually has an erratic and abnormal branching pattern.[1–3] Since photoacoustic systems can produce high-resolution, high-contrast images of vascular structures, they are now being developed for the study, diagnosis and monitoring of cancer and other vascular abnormalities. Although photoacoustic images of micro-vasculature can be produced in-vivo, fully reconstructing 3D micro-vascular images may require measurements from a large number of transducer locations, which can be time consuming and expensive. When the number of transducer locations is reduced, the system resolution, and hence the ability to view micro-vascular structures, is also reduced.

As it is difficult to fabricate high frequency transducer arrays that have the performance needed to image micro-vascular structures, it is often required that a single transducer element is mechanically scanned across a sample. CMUT technology[4,5] and Fabry-Perot transducers[6] may offer significant advantages to piezo-electric transducers, however there are still technological limitations in data acquisition. Furthermore, pulse repetition rates of lasers suitable for photoacoustic imaging are relatively slow and can impose excessive delays between subsequent measurements.[6] Before photoacoustic microscopy can be routinely applied to clinical examinations of micro-vasculature, technologies for rapidly processing and acquiring data from photoacoustic microscopes must be developed.

As an alternative to resolving microscopic vascular structures, *quantitative* methods that do not resolve individual structures can be used. Quantitative approaches specific to photoacoustic imaging based on measuring the blood oxygenation levels have already been developed.[7] In quantitative approaches, the effects pertaining to structural morphology of the tissue have been largely ignored or have been lumped together with other bulk tissue classification methodologies. In this work, analysis is provided regarding the effect that structural morphology has on photoacoustic signals. A method for simulating large scale photoacoustic models of vascular tissue is developed, which may find application in further related research.

To our knowledge, the use of a quantitative method for sub-voxel photoacoustic tissue classification by studying the effects of isolated structural parameters of vascular morphology has not been previously investigated. In addition, we are unaware of any published work involving large scale photoacoustic simulation of vascular networks or the reconstruction of images from such simulations.

Further author information: (Send correspondence to M.C.K.)
M.C.K.: E-mail: mkolios@ryerson.ca, Telephone: 1 416 979 5000 ext. 7065
J.Z.: E-mail: jzalev@ryerson.ca

Photons Plus Ultrasound: Imaging and Sensing 2011, edited by Alexander A. Oraevsky, Lihong V. Wang,
Proc. of SPIE Vol. 7899, 78992M · © 2011 SPIE · CCC code: 1605-7422/11/$18 · doi: 10.1117/12.873911

Our approach is based on the fact that vascular morphology in tissue can be modelled as a fractal process based on simple repetitive mathematical rules.[2,8,9] Such self similar fractal structures may have unique spatial-frequency characteristics that can be efficiently analysed by multi-scale wavelet methods.[10] It is known that photoacoustic signal responses are based on the spatial-frequency characteristics of the tissue.[11] Since fractal geometry can be used to model normal and abnormal vascular tissue, an approach using wavelet packet classification may be able detect sub-resolution vascular features from raw data prior to reconstruction.

In this work, we investigate using a functional classifier for detecting cancer and vascular disease through photoacoustic methods. Our work suggests that based on structural morphology alone, it is possible to distinguish between normal and abnormal vascular tissue using photoacoustic methods without reconstructing all of the vessel structures that contribute to the photoacoustic signal.

1.2 Advantages of Photoacoustic Imaging

In photoacoustic imaging, there are three main physical characteristics that give it a unique advantage for imaging vascular structures in tissue. First, the vascular images that are produced will endogenously have a natural high-contrast. This is because the light-absorption (and hence the photoacoustic signal strength) from blood is much greater than in the surrounding tissue. This causes the detected pressure wave from the blood vessels to be much stronger than from the other structures. This is contrary to standard pulse-echo ultrasound imaging, where blood vessels will usually have a low image contrast against the surrounding tissue.

Second, with photoacoustics, high-resolution is possible at greater depths than what is attainable using pure optical imaging methods. This is because the acoustic scattering in tissue is much less than the optical scattering. In tissue, photons cannot penetrate deeply without scattering, which has a blurring effect in other optical methods. In photoacoustic imaging, optical scattering can actually help in forming the image because it leads to a more uniform wide-field illumination of the tissue. However, since acoustic attenuation increases at high frequency, the maximum system resolution decreases with imaging depth. Photoacoustic microscopes can be used to image micro-vascular structures on the order of $10\mu\mathrm{m}$ and are even capable of resolving sub-cellular structures for small penetration depths.[12]

Third, since optical absorption is dependent on the wavelength of light, multi-wavelength photoacoustic systems can be used in functional imaging to measure molecular concentrations including blood oxygen saturation levels.[13] Hence, photoacoustic methods can detect regions of tissue with high blood concentration and high blood oxygenation that may indicate the presence of cancer.[7,13,14] This has been applied in approaches where the vessel structures are resolvable, and where the vessels structures are non-resolvable.

In addition, the laser pulses used in photoacoustic imaging are not a form of ionizing radiation, making it a safe imaging technology. In X-ray, CT, and PET, the patient is exposed to ionizing radiation that can damage DNA and has the potential to cause cancer.

2. PHYSICS OF PHOTOACOUSTIC IMAGING

2.1 Photoacoustic Waves

In photoacoustic imaging, a laser pulse heats an optically absorbing medium causing a rapid thermal expansion. This creates a source of pressure that propagates through the medium as an acoustic wave. Ultrasonic transducers that are positioned at several locations on the boundary of the medium are able to detect the acoustic wave as a time-domain photoacoustic signal, known as a *radio-frequency line* or an *RF-line*. Since the acoustic wave travels at the speed of sound ($\cong 1500\mathrm{m/s}$) through the medium, the RF-lines can be used to create a 3D spatial map proportional to the optical absorption strength of the medium.

In photoacoustic imaging, a very short laser pulse is used, so it is generally assumed that the system will be in *thermoelastic stress confinement*, where thermal conduction and stress propagation are negligible during the laser firing. Under this condition, an initial excess pressure will be created in the medium at time $t_0 = 0$ according to

$$p_0(\mathbf{x}) = \Gamma(\mathbf{x})\mu_a(\mathbf{x})\Phi(\mathbf{x}), \tag{1}$$

where $\mu_a(\mathbf{x})$ is the optical absorption profile of the medium and $\Phi(\mathbf{x})$ is the energy fluence from the laser. The parameter $\Gamma(\mathbf{x}) = \frac{\beta(\mathbf{x})c^2(\mathbf{x})}{C_p(\mathbf{x})}$ is known as the Grüneisen parameter, where $\beta(\mathbf{x})$ is the thermal expansion coefficient, c is the speed of

sound and $C_p(\mathbf{x})$ is the specific heat capacity. If the laser pulse is instantaneous, and the medium is homogenous with a constant speed of sound, then the wave propagation is governed by the differential equation

$$\left(\frac{\partial^2}{\partial t^2} - c^2\nabla^2\right) p(\mathbf{x},t) = p_0(\mathbf{x})\frac{\partial}{\partial t}\delta(t), \tag{2}$$

where $p(\mathbf{x},t)$ is pressure and $\delta(t)$ is the Dirac impulse function. Solving Eqn. (2) under basic assumptions yields the *forward solution* for $p(\mathbf{x},t)$. If the laser is fired at t_0, the pressure at any time and position is determined by

$$\begin{aligned} p(\mathbf{x},t) &= \frac{\partial}{\partial t}\int g(\mathbf{x}-\mathbf{x}',t)p_0(\mathbf{x}')\,d\mathbf{x}' \\ &= \frac{\partial}{\partial t}\Big(g(\mathbf{x},t) * p_0(\mathbf{x})\Big), \end{aligned} \tag{3}$$

where $g(\mathbf{x},t) = \frac{1}{c^2}\frac{\delta(\|\mathbf{x}\|-ct)}{4\pi\|\mathbf{x}\|}$ is the *Green's function solution* of Eqn. (2).

2.2 Resolution and Penetration Depth

Laser light has limited penetration depth in tissue. This introduces a limit on how deep an absorber can be detected photoacoustically in tissue. Furthermore, attenuation of an acoustic wave increases at high frequencies so this places a further limit on the depth penetration, with high-resolution systems being able to penetrate less deeply.

The *resolution* of an imaging system is the minimum distance that two objects must be spaced apart to be detected as separate objects. The *axial resolution* for photoacoustic imaging is given by $\varrho_{\text{axial}} = 2a_{\text{min}} \approx 3\frac{c}{f_{\text{max}}}$, where f_{max} is the maximum cutoff frequency of the ultrasound transducer and a_{min} is radius of the smallest spherical absorber that can be resolved. The *lateral resolution* for a curved transducer array is given by $\varrho_{\text{lateral}} \approx 1.22\frac{\lambda_{ac}}{\arcsin(D/z)} \approx a_{\text{min}}\frac{z}{D}$, where λ_{ac} is the smallest detectable acoustic wavelength, z is the radius of curvature of the transducer and D is the aperture radius.[15]

In general, as the number of sampled transducer locations becomes increasingly sparse, it becomes more difficult to maintain the same resolution. This is partially because when transducer elements are spaced too far apart, sidelobe distortions will form when the image is reconstructed.[16] The ratio of the side lobe power to the main lobe power is proportional to $1/N$, where N is the number of transducers.[16] The ratio needs to be as small as possible to accurately reconstruct images without such artifacts.

For reconstructing high-resolution images, a large number of transducer locations must be sampled. It is known that the information content of a transducer signal is related to the frequency response and field profile of the transducer. However, as the number of transducer sampling locations becomes sparse, thereby reducing the system resolution, the information content from each individual signal remains the same. In our approach, we exploit this fact to classify tissue even when the structures are not resolvable.

Furthermore, the frequency content of the received signal in photoacoustic imaging is not related linearly to frequency content a transmit pulse as it is in pulse-echo ultrasound imaging. Hence, photoacoustic signals have wide-band frequency content that allows features at multiple scales to be detected.

3. VASCULAR GEOMETRY

Tumors are structurally abnormal at the cellular and tissue levels. As with normal tissue, tumors require oxygen, nutrients, and must remove waste. However, they contain abnormal and disfunctioning blood vessels and greatly differ in appearance from normal vessels. Often regions inside of the tumor may be hypoxic having reduced oxygen levels, which may be detected using photoacoustic methods. To gain oxygen and nutrients, a tumor cell may begin to induce its own blood supply. The tumor may form blood vessels from existing capillaries or may grow around other blood vessels. These changes are due to the release of growth factors such as VEGF, FGF and IL-8 that affect the vasculature physiologically and morphologically.[1,17–21]

Tumour vessels have a high *tortuosity*, which is a measure of the curvyness of the vessels.[1,17] Vascular morphology can be characterized by analysing the properties of vessels from a structural point of view. *Vessel segmentation* and *centerline extraction* can be used to extract the paths of vessels from a reconstructed image of vascular tissue. If a reconstructed image

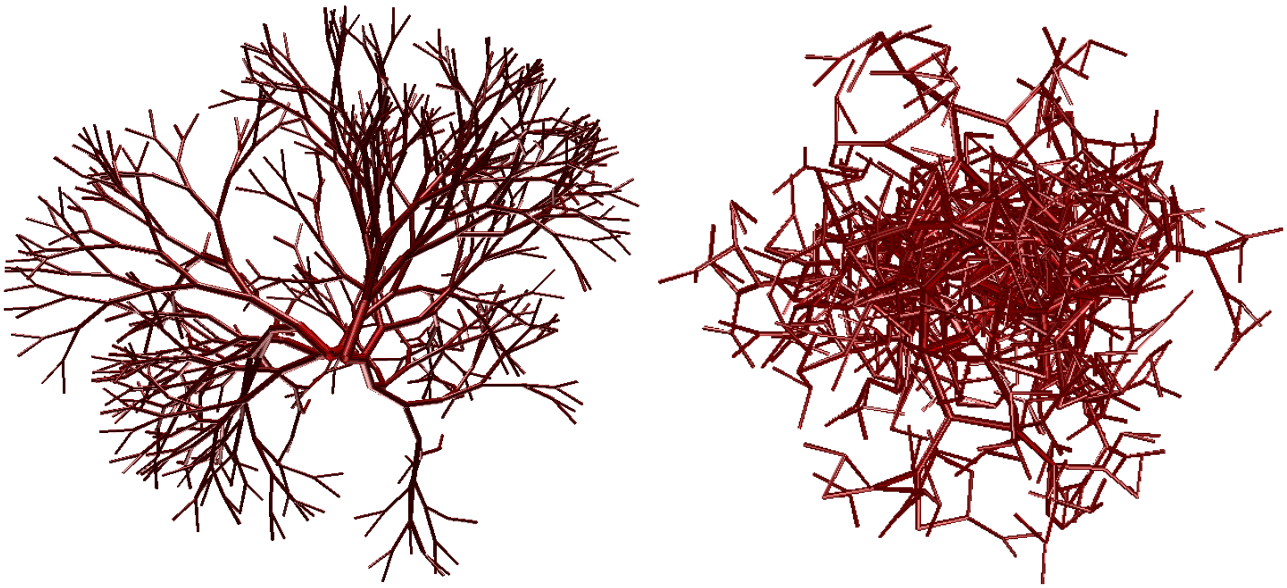

(a) Normal Tissue (b) Abnormal Tissue

Figure 1. Simulated vascular tissue geometry. For normal tissue, the branch angle range varies from 25°to 27°. For abnormal tissue, it varies from 25°to 140°.

has the resolution to resolve individual vessels, metrics can be evaluated to characterize or discriminate between normal and abnormal vasculature. These metrics include the *vessel count*, which is the number of individual vessels contained within a region of interest; the *average radius* of vessels within a region of interest; the *branching angle distribution* of vessel segments; the *average vessel length*; the *sum-of-angles*, where the change in angle between successive vessel tangents are added together at regular intervals along a vessel path; and the *inflection count measure* which is related to the number of maxima on the vessel path.[22] When the vessel structure cannot be resolved these metrics cannot be directly evaluated, although their effects can still be modelled.

There are numerous methods for generating and representing models of vascular structures in tissue.[2,3,23–28] The goal of these approaches is to emulate the tissue with parameters based on actual physical manifestations of vascular tissue. Several works have used *fractal trees* to model vascular tissue.[2,3] A fractal tree is a mathematical structure that is formed by iteratively applying a statistical branching pattern to generate the large scale object (see Figure 1). In Ref. 3 renal vascular tissue is modelled a fractal tree consisting of many branching vessel segments. In Ref. 2, fractal trees are used to study the flow of ultrasound contrast agents moving through normal and abnormal renal vascular tissue. Our method for generating vascular trees to examine photoacoustic effects due to changes in structural morphology is based on the fractal tree approach and is described in Section 5.1.

4. CLASSIFICATION ALGORITHM

Tissue characterization is the process of determining which of several classes of tissue a particular sample belongs. For example, tissue characterization could involve determining if a sample of tissue is healthy or diseased or if it is muscle tissue or adipose tissue. *Tissue segmentation* is the process of outlining the boundaries and measuring sizes of tissue regions and structures. Tissue characterization is related to tissue segmentation; however, in tissue characterization, boundaries do not need to be detected. In tissue segmentation, the tissue does not need to be identified or diagnosed.[29] Most ultrasound image segmentation methods are developed from B-mode (log-compressed) images and not unprocessed RF-signals Tissue characterization is most often done on the RF signal or envelope-detected RF signal.[29,30]

Our tissue classification algorithm is broken down into two phases that are shown in Figure 2. Phase I, is the *training phase*, where a classifier is learned from a *training set* of measurements representative of the data. In Phase II, the *testing phase*, the learned classifier is used to discriminate between measurements in a *test set* that were not necessarily encountered during the training phase.

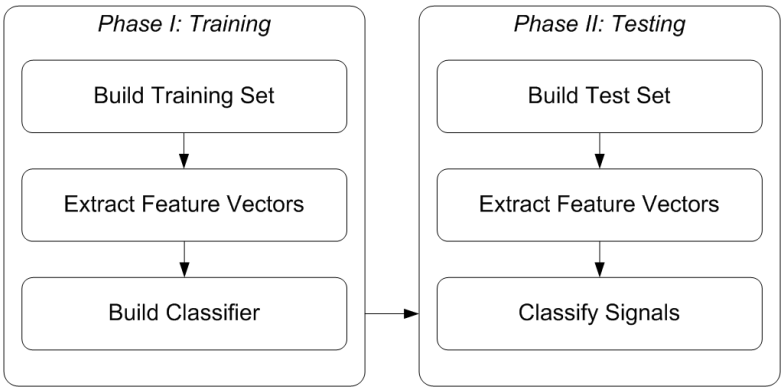

Figure 2. Phases of classification algorithm. Phase I, is the *training phase*, where a classifier is learned from a set of measurements representative of the data. In Phase II, the *testing phase*, the learned classifier is used to discriminate between measurements that were not necessarily encountered during the training phase.

Our method makes use of the Support Vector Machine (SVM) algorithm, which is a common method used to produce a classifier from a set of initial measurements that either *belong* or *do-not-belong* to a specific category defined for the problem at hand. This learned classifier can then be used to test if any future measurement belongs to the specific category. The set of N examples

$$V_{\text{training}} = \{(\mathbf{z}_1, y_1), \ldots, (\mathbf{z}_N, y_N)\} \tag{4}$$

used to train the classifier is known as the *training set*. It describes the initial measurements that are used for training the SVM classifier. Each example $(\mathbf{z}_i, y_i)$ contains a *feature vector* $\mathbf{z}_i \in \mathbb{R}^n$ consisting of n values that describe a single measurement. The binary value $y_i \in \{-1, +1\}$ is called a *class label*. It is assigned to each example and signifies if the feature vector $\mathbf{z}_i$ is a member of the specific category defined for the problem. It is assigned values by the rule

$$y_i = \begin{cases} +1 & \text{if } \mathbf{z}_i \text{ belongs to the category} \\ -1 & \text{if } \mathbf{z}_i \text{ does not belong to the category} \end{cases} \tag{5}$$

The SVM attempts to solve an optimization problem to construct a best-fit classifier based on the *decision function*

$$f_{\boldsymbol{\alpha}}(\mathbf{z}) := \operatorname{sgn}\left(\sum_{i=1}^{N} y_i \alpha_i K(\mathbf{z}, \mathbf{z}_i) + b\right), \quad f_{\boldsymbol{\alpha}} : \mathbb{R}^n \to \{-1, 1\} \tag{6a}$$

where $\boldsymbol{\alpha} = (\alpha_1, ..., \alpha_l)$ is a *weight vector*, b is a *bias constant*, N is the number of examples, $\operatorname{sgn}(x)$ is the signum* function, y_i is the class label and $K(\mathbf{z}, \mathbf{z}_i)$ is a chosen *kernel function*. The term

$$\sigma_{\boldsymbol{\alpha}}(\mathbf{z}) := \sum_{i=1}^{N} y_i \alpha_i K(\mathbf{z}, \mathbf{z}_i) + b \tag{6b}$$

inside the brackets of Eqn. (6a) is called the *classification strength*. It represents the strength of the classifier for any particular feature vector $\mathbf{z}$ being tested. The vector $\boldsymbol{\alpha}$ in Eqn. (6a) can be manipulated allowing $f_{\boldsymbol{\alpha}}$ to constitute a wide range of possible functions. This is the mechanism for tuning the classifier. The range of decision functions $f_{\boldsymbol{\alpha}}$ that are possible depends the *kernel function* K that is selected. The *linear kernel*, $K_{\text{linear}}(\mathbf{z}, \mathbf{z}_i) = \mathbf{z} \cdot \mathbf{z}_i$, and the *Gaussian radial basis function kernel*, $K_{\text{GRBF}}(\mathbf{z}, \mathbf{z}_i) = e^{-|\mathbf{z}-\mathbf{z}_i|^2/\kappa}$, are common choices for the kernel function. K_{GRBF} may be used when feature vectors exist in clusters that are not cannot be discriminated using K_{linear}. In this work, the SVM solver software *SVMPerf*[31] is used with the K_{GRBF} kernel.

The Wavelet Packet Transform (WPT) is often used in classification algorithms, where its output is generally used to create a feature vector.[32–35] In discrete wavelet methods, a low-pass filter $h[n]$ is selected so that its z-transform $H(z)$

*The signum function is defined by $\operatorname{sgn}(x) = \begin{cases} +1, & x \geq 0, \\ -1, & \text{otherwise.} \end{cases}$

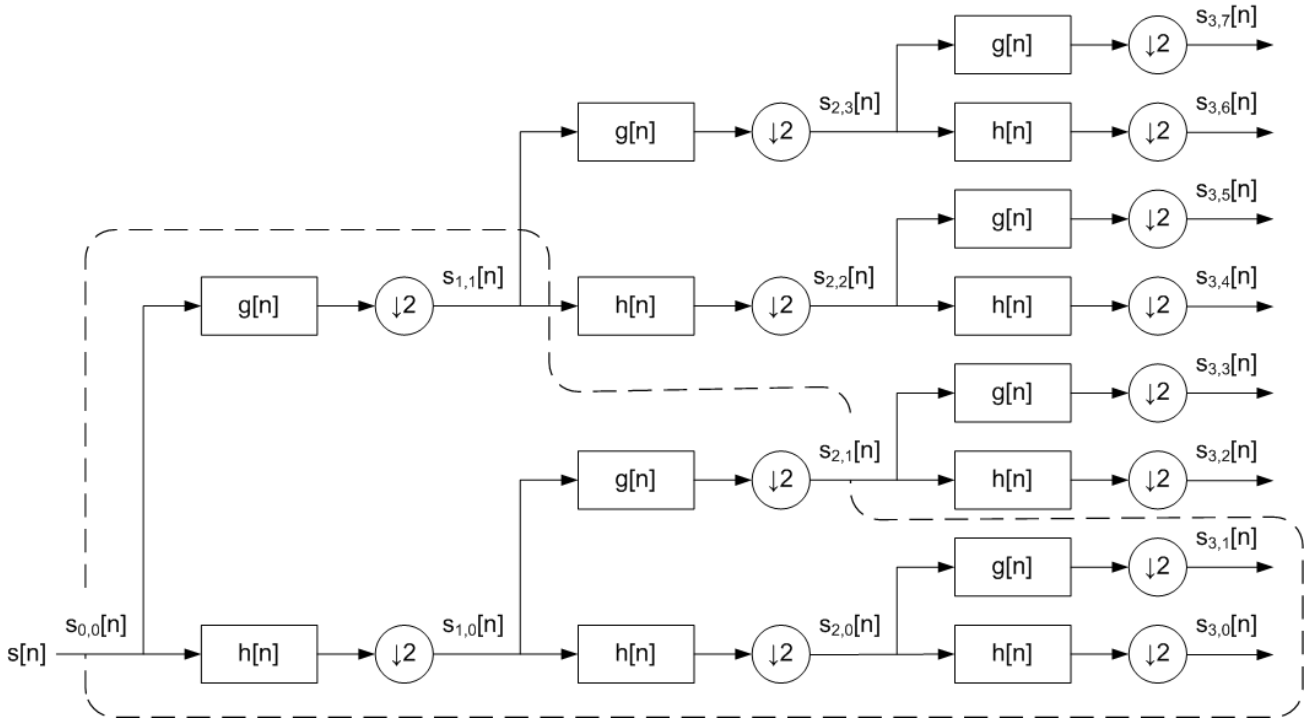

Figure 3. The Wavelet Packet Transform (WPT) decomposition filters. The $h[n]$ blocks are the low-pass filters and $g[n]$ blocks are the high-pass filters. The signals $s_{p,q}[n]$ are shown as output from each stage of the WPT for $p = 0..3$, $q = 0..2^p - 1$. Applying an information cost function $C(\mathbf{u})$ to each output channel produces a scalar feature in the feature vector. The dotted line indicates the boundaries of the Discrete Wavelet Transform (DWT).

satisfies the *quadrature mirror condition* $H(z)H(z^{-1}) + H(-z)H(-z^{-1}) = 1$. A corresponding high-pass filter $g[n]$ is then defined by its z-transform such that that $G(z) = zH(-z^{-1})$. In the WPT, a signal is processed through a cascaded filterbank of high-pass filters, low-pass filters and down-sampling operations as shown in Figure 3. The WPT can be thought of as an extension of the Discrete Wavelet Transform (DWT). In Figure 3, the DWT component of the WPT is shown surround by a dotted line. The wavelet packet decomposition of a signal $s[n]$ is recursively defined as[32]

$$s_{p+1,2q}[n] := \sqrt{2}(h * (s_{p,q})_{\downarrow 2})[k] = \sqrt{2}\sum_k h[k]s_{p,q}[2n-k]\,, \tag{7a}$$

$$s_{p+1,2q+1}[n] := \sqrt{2}(g * (s_{p,q})_{\downarrow 2})[k] = \sqrt{2}\sum_k g[k]s_{p,q}[2n-k]\,, \tag{7b}$$

where $s_{p,q}[n]$ is the WPT decomposition output of each stage for $p \in \mathbb{Z}^+$ and $q = 0..2^{p-1}$ and $s_{0,0}[n] := s[n]$.

The WPT is not shift-invariant. This means that a single sample delay could significantly alter its output which can have an impact on its pattern classification ability. By making use of separate real and complex filter banks, as in the Dual-Tree Complex Wavelet Packet Transform (DTCWPT),[36] it is possible to gain nearly ideal shift-invariance. The DTCWPT guarantees filters with analytic properties that can be used to effectively extract the envelope of a wavelet packet.

The *hilbert transform* of a function is defined as

$$\begin{aligned}\mathcal{H}\{f(t)\} &= \frac{1}{\pi t} * f(t) \\ &= \mathcal{F}^{-1}_{\omega\to t}\big\{ j\,\mathrm{sgn}(\omega)\mathcal{F}_{t\to\omega}\{f(t)\}\,\big\}\end{aligned} \tag{8}$$

The *envelope amplitude* and *envelope phase* can be extracted from the hilbert transform by

$$\mathcal{H}^{\text{env}}\{f(t)\} = |f(t) + j\mathcal{H}\{f(t)\}|, \tag{9a}$$

$$\mathcal{H}^{\Phi}\{f(t)\} = \tan^{-1}\left(\mathcal{H}\{f(t)\}\,, f(t)\right). \tag{9b}$$

In the complex dual-tree approach, an additional imaginary filter tree duplicates real filter tree of Figure 3. In the imaginary tree, the real high- and low-pass filters $h[n]$ and $g[n]$ from the DWT block (inside the dotted line in Figure 3) are replaced with their hilbert transforms $h'[n] := \mathcal{H}\{h[n]\}$ and $g'[n] := \mathcal{H}\{g[n]\}$. The extension filters (outside of the dotted line in Figure 3) must be equal for the real and imaginary trees, but may be different from the filters in the DWT section. The input to the imaginary filter tree is given an additional one sample delay as a pre-filter to meet the requirements giving analytic signal properties. The outputs after each block in the real and imaginary filter trees are denoted by $s^{\Re}_{p,q}[n]$ and $s^{\Im}_{p,q}[n]$. Due to the analytic properties of the transform, an envelope and phase analogous with Eqn. (9) can be defined as $s^{\text{env}}_{p,q}[n] = |s^{\Re}_{p,q}[n] + j s^{\Im}_{p,q}[n]|$ and $s^{\Phi}_{p,q}[n] = \tan^{-1}(s^{\Im}_{p,q}[n], s^{\Re}_{p,q}[n])$.

In both the training phase and the testing phase of our algorithm, feature vectors are constructed from the sampled transducer RF signals. The entire transducer signal $s(t)$ undergoes dual-tree wavelet packet decomposition. The feature vector, designated $\mathbf{z}_{s(t)}$, is created on a sliding window in the transducer signal centered at time t. A window sampling duration T_w is defined, where the number of DTCWPT samples in the window is $N_w = T_w/\Delta t$ and Δt is the period of each sample. From the output of the sampling window, a feature vector $\mathbf{z}_i$ of length 2^p is created by applying an information cost function to each of the 2^p wavelet packets. The feature vector for level p, noted $\mathbf{z}^p_{s(t)}$, is creating by applying an information cost function $\mathcal{C}(\mathbf{u})$ to each of the $q = 2^p - 1$ packet envelopes $s^{\text{env}}_{p,q}[n]$ according to

$$\begin{aligned} \mathbf{z}^p_{s(t)} &= \{\mathcal{C}(\mathbf{u}_q) \,:\, q = 1 \,\ldots\, 2^p - 1\}\,, \\ \mathbf{u}_q &= \left\{ s^{\text{env}}_{p,q}[n] \,:\, n \in \left[\lceil \frac{t/\Delta t}{2^p} \rceil, \lceil \frac{t/\Delta t + N_w}{2^p} \rceil \right] \right\}. \end{aligned} \tag{10}$$

The feature vector is then taken as $\mathbf{z}_{s(t)} := \mathbf{z}^p_{s(t)} = (z^{p,0}_{s(t)}, z^{p,1}_{s(t)}, \ldots, z^{p,2^q-1}_{s(t)})$. Hence, a feature vector $\mathbf{z}_{s(t)}$ is the ordered set consisting of the information cost function applied to a window centered at t on each packet envelope. We thus have specified a feature vector that can be constructed at any value of t. For this work the log-energy cost function $\mathcal{C}(\mathbf{u}) = \sum_i^{u_i \neq 0} \ln u_i^2$ is used. Other information cost functions are described by Ref. 32 and Ref. 35 can also be used.

To train the classifier, M transducer signals are obtained from a set of measurements representative of photoacoustic signals that would be encountered during regular use. For each transducer signal $s_m(t)$, $m = 1 \ldots M$, there are N_m window positions centered at τ_{mn}, $m = 1 \ldots M$, $n = 1 \ldots N_m$, that are spaced apart by T_{step}, where $\tau_{mn} = \tau_{m0} + (n-1)T_{\text{step}}$. The class labels y_m from Eqn. (5) are assigned the value +1 for normal tissue, and -1 for abnormal tissue. The training set Eqn. (4) that we use is now written

$$V_{\text{training}} = \{(\mathbf{z}_{s_m(\tau_{mn})}, y_m) \,:\, m = 1 \ldots M,\; n = 1 \ldots N_m\}, \tag{11}$$

where $\mathbf{z}_{s_m(\tau_{mn})}$ is obtained from Eqn. (10).

To improve the performance in the presence of noise, an approach similar to Ref. 34 is used. Prior to commencing the algorithm, several feature vectors $\mathbf{z}_{\text{noise},i}$ are generated from pure white-noise. An average noise vector $\bar{\mathbf{z}}_{\text{noise}} = \frac{1}{N}\sum_i \mathbf{z}_{\text{noise},i}$ is then calculated. Each feature in $\mathbf{z}$ is thus normalized by the corresponding feature in $\bar{\mathbf{z}}_{\text{noise}}$. In addition, to ensure that all packets have the same energy, each feature vector is also normalized by $\mathbf{z}' = \mathbf{z}/\|\mathbf{z}\|$.

5. SIMULATION

Photoacoustic transducer signals from vascular tissue are studied in two ways. The first method involves generating large-scale models of normal and abnormal vascular tissue using fractal trees and simulating the photoacoustic response from each tree. The second method involves using actual 3D tissue geometry of micro-vasculature obtained using optical coherence tomography (OCT) and simulating the photoacoustic response from these datasets.

5.1 Fractal Tree Model

Simulation of vascular networks using fractal trees is a convenient method for generating datasets of vascular tissue. The mathematical structure of the fractal tree model allows specific morphological parameters to be varied in a deliberate way which is beneficial for performing controlled testing. Parameters such as the *branching angle distribution*, the *average vessel length* and the *average vessel radius* can thus be isolated and studied. In our work, the most significant structural

parameter that is studied is the branching angle distribution. The criteria used to describe normal and abnormal tissue are based on Ref. 2. Normal tissue is modelled with uniformly distributed branching angles ranging from 25-27°and abnormal tissue is modelled with branching angles ranging from 25-140°as shown in Figure 1.

Although a fractal tree is only an approximation for real tissue, it is assumed that the parameters used for generating the fractal tree will be sufficient to study the parameters we are interested in. Furthermore, the parameters used are based on renal tissue; however, it is assumed that the ability to discriminate abnormal from normal will translate to other types of tissue that can be generated from different morphological parameters.

In the model, we assume that the optical properties of the tissue follow the wide-field photoacoustic assumption where the entire tissue is illuminated everywhere uniformly from a single laser pulse. It is assumed that blood is the only absorber in tissue so that $\mu_{a,\text{blood}} \gg \mu_{a,\text{tissue}} \approx 0$. The optical absorption profile is therefore given by

$$\mu_a(\mathbf{x}) = \begin{cases} \mu_{a,\text{blood}}, & \text{if } \mathbf{x} \text{ is in a vessel,} \\ 0, & \text{otherwise.} \end{cases} \tag{12}$$

The laser energy fluence can be set to the constant $\Phi(\mathbf{x}) = {}^{C_p}/_{\beta c^2 \mu_{a,\text{blood}}}$ so that the initial excess pressure $p_0(\mathbf{x})$ of Eqn. (1) is either 0 or 1.

Each transducer is modelled as an ideal omni-directional point detector that measures a pressure signal at a given position with respect to time. The photoacoustic signal produced by the tissue can be found from Eqn. (3). A 3^{rd}-order Butterworth filter with a 3dB cutoff frequency of 250MHz is applied to each transducer signal to approximate the frequency response of an actual high-frequency transducer.

Our photoacoustic simulator operates on a fractal tree with cylindrical-segment geometry. Each cylindrical vessel segment has a defined start position, end position and vessel diameter to completely specify the fractal tree geometry. By simulating the signal directly from the fractal tree geometry, the entire matrix of points for the region-of-interest does not need to be stored in computer memory for the simulation. This allows a more efficient simulation with higher resolution than would otherwise be possible with the same CPU resources. To form the photoacoustic signal, each cylinder is broken down into many individual photoacoustic point sources. The distance of each point source to the transducer is then calculated. Using Eqn. (3) the contribution from each photoacoustic point source is added to the photoacoustic signal. To allow the spatially separated point sources to better approximate a solid object, a smoothing filter $h[t]$ can be applied such that $h[t] = (\cos(2\pi t/n_h - \pi) + 1)/2$ for $t = 0 \,..\, n_h - 1$ with $n_h = 2\lfloor 3\Delta l/(c\Delta t)\rfloor$ and where Δl is the expected value of the distance between point sources. Figure 4 shows one configuration used for simulating photoacoustic signals from the fractal vascular geometry.

To validate this photoacoustic simulator, a separate FEM simulation of individual vessel segments was used to compare output. The FEM models were not suitable for large scale tissue simulation due to high computational requirements. Also, an exact equation was derived to model photoacousitc signals produced by finite-length cylinderical segments and the results were shown to be in agreement.[37]

5.2 Acquired 3D Vascular Geometry

In the second tissue model, photoacoustic signals are simulated from the actual geometry of 3D datasets of micro-vasculature obtained in-vivo from mouse skin using optical coherence tomography[38] †. These datasets contain the geometry of the micro-vessels with very high contrast and resolution. Figures 5a and 5b show cross-sections of these datasets for normal tissue and abnormal tissue with a cancerous tumor. Each dataset is $800 \times 800 \times 128$ voxels encoded as 256 shades of grey. The OCT imaging method can examine the tissue up to a depth of 2 mm. We have preprocessed the datasets with a sigmoid thresholding procedure to make vessel structures have a more uniform heat absorption profile for photoacoustic simulation. The thresholding function $f(x) = 1 + \arctan(ax + b)/\pi$ was used where a and b are constants chosen to maximize the vessel contrast. Since the 3D dataset is rasterized, the photoacoustic signal produced by the tissue can be generated by applying Eqn. (3) and treating each voxel as a separate photoacoustic point source.

† 3D datasets courtesy of A. Mariampillai and A. Vitkin, Princess Margaret Hospital, Toronto, ON

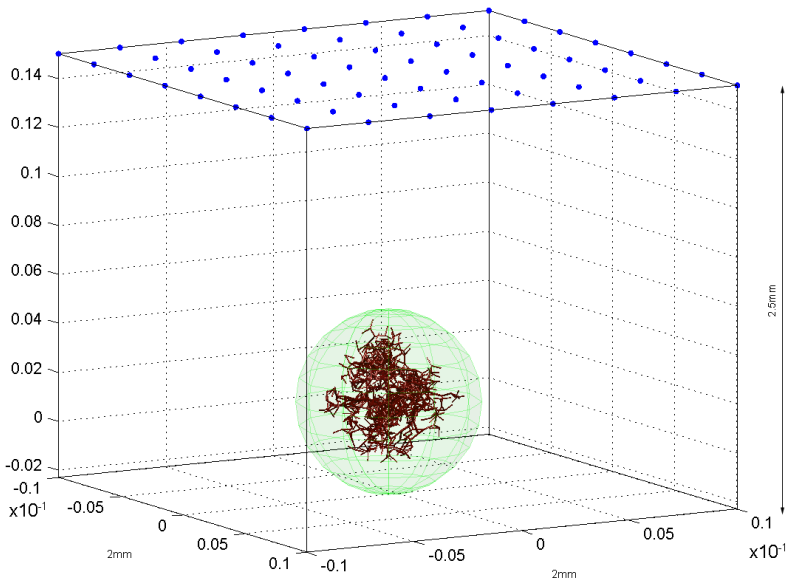

Figure 4. Configuration used in the point detector simulation. Planar array $n_x = 8, \quad n_y = 8$

6. RESULTS

6.1 Performance of the Classifier using Fractal Vascular Model

The fractal tissue model was used to test if changes in the branching angle in vascular tissue would result in detectable changes in photoacoustic signals. To train the classifier, 16 simulated trees for each of 9 different vascular geometry configurations were generated. The 9 vascular configurations (DS-SIM1 to DS-SIM9) contained increasingly greater variation in the branching angle distribution. The allowed the simulation of a continuous range of vascular abnormality spanning from very healthy tissue to very abnormal tissue. By continuously varying the amount of vascular abnormality, a stronger and more robust classifier for detecting between the normal and abnormal categories could be produced.

64 transducers were simulated as shown in Figure 4 for each of the $9 \times 16 = 144$ fractal trees. For each RF-line measurement, a window size corresponding to a distance of $256\mu\text{m}$ is selected, with a step size corresponding to $128\mu\text{m}$. This results in 64 sampling windows per transducer signal. Windows where the simulated data had zero signal were dropped. In all, the training set consisted of over 10000 feature vectors. The filter level $p = 6$ was chosen and the feature vector thus had $2^6 = 64$ features. Feature vectors corresponding to measurements from DS-SIM1 through DS-SIM3 were assigned SVM class labels $y_m = +1$ to indicate normal tissue. Measurements from DS-SIM4 through DS-SIM9 were assigned $y_m = -1$ to indicate abnormal tissue. The SVM classifier was created using the *SVMPerf* solver of Ref.31. The quality of the solution is related to the run-time duration of the solver. The maximum solver run-time was set to 15 minutes.

To test the performance of our algorithm on the normal and abnormal vasculature, four fractal trees for normal tissue and four fractal trees for abnormal tissue were generated to make up the test set. From each tree, 7 of the transducer signals were selected at random. Feature vectors were created in the same manner as they were for the training set. The output from the SVM decision function is evaluated using Eqn. (6). The results are shown in Table 1. The *sensitivity* and *selectivity* of the algorithm are calculated as

$$\text{Sensitivity} = \frac{\text{True Positives}}{\text{True Positives} + \text{False Negatives}}, \qquad \text{Selectivity} = \frac{\text{True Negatives}}{\text{True Negatives} + \text{False Positives}}. \tag{13}$$

To test if the two classes are distinguishable using Eqn. (6), the Welsh test[39] was used to calculate Hotelling's T^2 statistic for two independent samples with unequal variances. The p-value corresponding to the T^2 statistic is also calculated. The p-value indicates the probability that the *null hypothesis* is true, which is that the mean classifier strength for each class is not significantly different. If the p-value is less than 5% then it will be concluded that the null hypothesis is false and therefore the classes are distinguishable.

To examine the performance of the classification algorithm in the presence of noise, white noise is added to each transducer signal in the test set. Signal to noise ratios +30dB, +10dB, +3dB and -3dB are used. As the noise increases, the performance is reduced. At +10dB SNR, some normal tissue is weakly classified as abnormal. At +3dB SNR, the classifier cannot detect any abnormal tissue. The p-value shows that the resulting difference has a high probability of being not significant for +3dB and -3dB. The result is significant for +30dB and +10dB.

From Table 1 it can be seen that a classifier can be constructed that will discriminate between photoacoustic signals of the normal and abnormal tissue models and that noise reduces the performance of the algorithm. With no noise the classifier performs with a sensitivity of 96.4%, a selectivity of 78.6% and a p-value of 0.0039%. With a SNR of +30dB the classifier performs with a sensitivity of 96.4%, a selectivity of 85.7% and a p-value of 0.0000%. With a SNR of +10dB the classifier performs with a sensitivity of 60.7%, a selectivity of 89.2% and a p-value of 0.0007%. However, when the SNR is only +3dB the classifier performance is greatly reduced with a sensitivity of 100%, a selectivity of 0% and a p-value of 10.4%. At -3dB the classifier performs with a sensitivity of 100%, a selectivity of 0% and a p-value of 100%.

6.2 Performance of the Classifier using Actual 3D Vascular Geometry

The acquired 3D data was tested in a C-scan configuration, to simulate an actual tissue microscopy scan. The tissue datasets are $5\text{mm} \times 5\text{mm} \times 0.2\text{mm}$ in size. The tissue is scanned across many positions in the xy plane and at each position, a subregion of the tissue is illuminated using the Gaussian fluence profile as shown in Figure 6a and 6c. At each scan position in the xy-plane, the laser pulse illuminates a $1.2\text{mm} \times 1.2\text{mm} \times 0.2\text{mm}$ sub-region of the tissue. Four transducers located 0.56mm from the center of the laser detect the photoacoustic signal for each sub-region. The tissue is scanned in the x and y directions at $17 \times 17 = 289$ positions.

To observe the ability of the 4 transducers to reconstruct the geometry in a sub-region, a reconstruction of an image slice is performed (Figure 6d). A similar reconstruction using 256 transducers is also performed (Figure 6e). It is seen that the sparse four transducer arrangement is not sufficient to reconstruct the 3D gemoetry, however, the dense 256 transducer arrangement can accurately reconstruct the geometry.

The classifier is trained using 10% of the transducer signals from a sub-region of normal tissue and abnormal tissue. Normal tissue is assigned $y_m = +1$, abnormal tissue is assigned $y_m = -1$.

The average classifier strength of Eqn. (6) from each transducer is mapped into the 2D C-scan locations and used to create 2D parametric maps of the classifier (Figure 5).

SNR	TN	FP	FN	TP	Sensitivity	Selectivity	T^2	p-value
Original	22	6	1	27	96.4%	78.6%	16.88	0.0039%
+30 dB	24	4	1	27	96.4%	85.7%	104.77	0.0000%
+10 dB	25	3	11	17	60.7%	89.2%	20.16	0.0007%
+3 dB	0	28	0	28	100%	0%	2.64	10.4134%
-3 dB	0	28	0	28	100%	0%	0.00	100.0000%

Table 1. Sensitivity and selectivity of the classifier. The T^2 test for two independent samples with unequal variances and the corresponding p-value are calculated. The p-value indicates the probability that the two classes have no classifiable difference. A p-value less than 5% will indicate a statistical significance.

Figure 5 shows a 2D C-scan style parametric plot of the classifier strength. This shows that the abnormal tissue can be discriminated from the normal tissue where it is not possible to reconstruct the image using the same transducer arrangement. Figure 6d and Figure 6e show that when only 4 transducers are used, the ability to reconstruct a 2D slice of tissue is not possible, although when 256 transducers are used the vasculature can be reconstructed. To test if the classifier is able to detect a significant pattern between the two cases, the T^2 test for two independent samples with unequal variance is calculated to be $T^2 = 1259.9$. This corresponds to a p-value of 0.00% which shows that the two datasets are significantly different.

7. DISCUSSION

In this work, it has been demonstrated how a classifier can be constructed to photoacoustically discriminate between tissue with different structural morphology. A change in the branching angle resulted in a detectable change in the wavelet packet

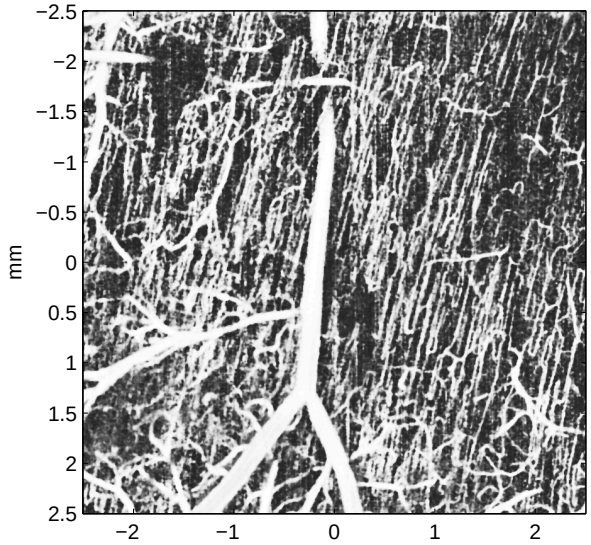

(a) Normal tissue cross-sectional slice at depth $= 0.875\mathrm{mm}$

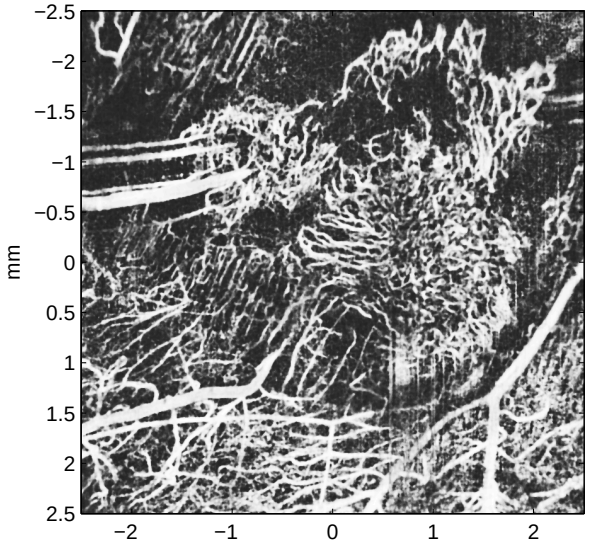

(b) abnormal tissue cross-sectional slice at depth $= 0.875\mathrm{mm}$

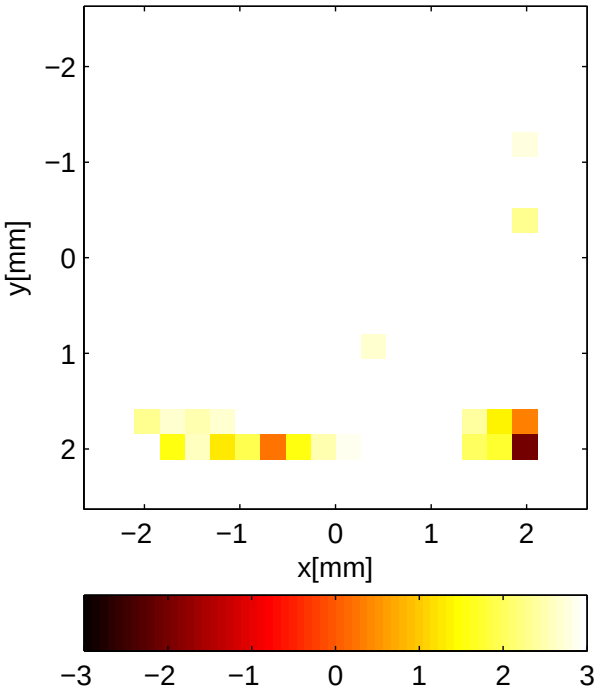

(c) Classifier strength on normal tissue

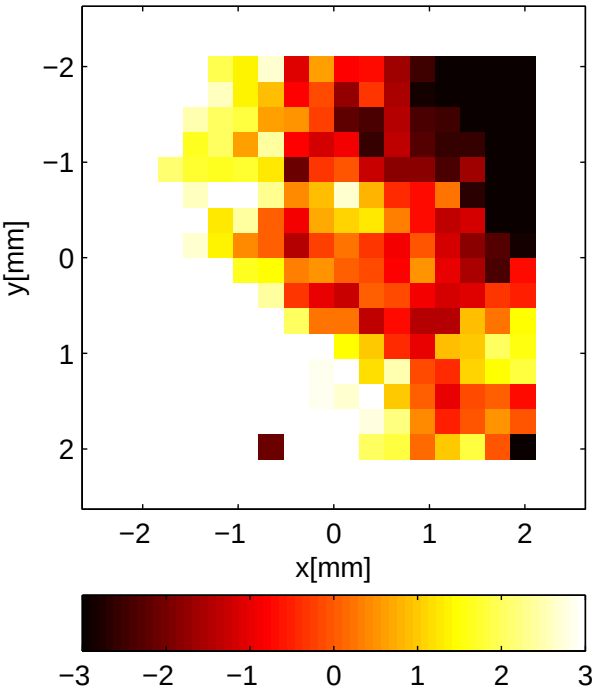

(d) Classifier strength on abnormal tissue

Figure 5. Classification of acquired 3D data. (a)-(b) 2D cross-sectional slices of the of the 3D micro-vascular tissue datasets. (c)-(d) Parametric images of classifier strength applied to photoacoustic signals from C-scan of the 3D tissue as described in Figure 6. There were 289 C-scan sub-regions simulated. Each sub-region is simulated with data from only 4 transducers, which is not enough information to resolve the vascular structures. The classifier was trained on a subset of the recorded data from each tissue type.

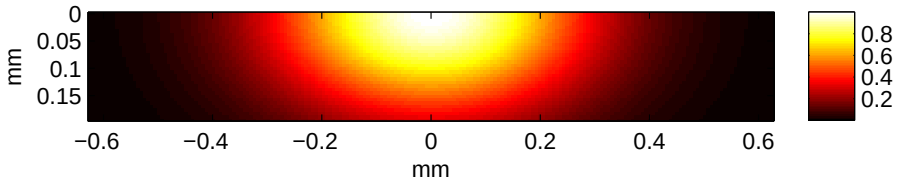

(a) Gaussian laser fluence profile (side view)

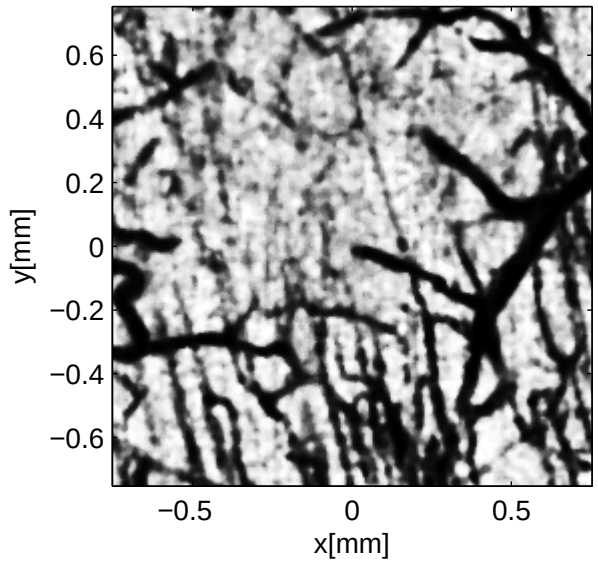

(b) $1.5 \times 1.5\mathrm{mm}^2$ cross-section of healthy tissue sub-region at depth $= 0.1\mathrm{mm}$.

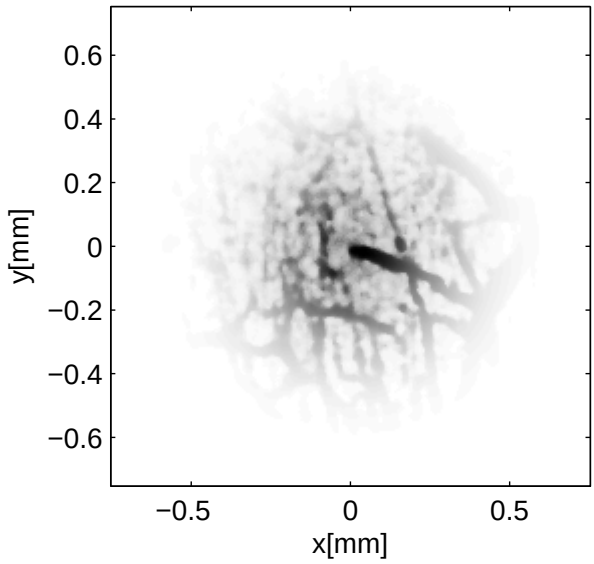

(c) sub-region illuminated by Gaussian profile

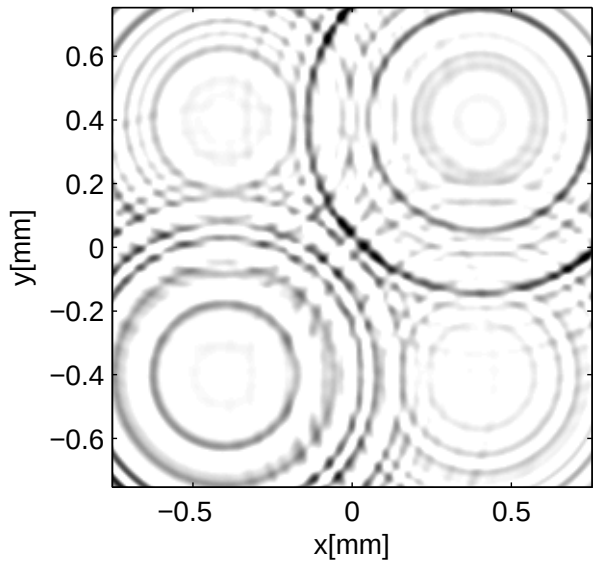

(d) reconstruction of the subregion using 4 transducers

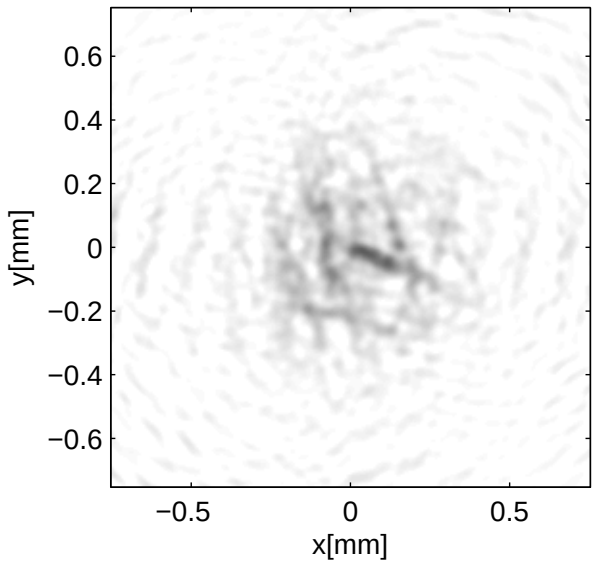

(e) reconstruction of the subregion using 256 transducers

Figure 6. Simulated 3D reconstruction of a tissue sub-region using a limited number of transducers. (a) The Gaussian optical illumination profile used to illuminate a 3D tissue sub-region. (b) A 2D cross-sectional slice of the 3D sub-region. (c) The initial pressure at $t = 0$ generated by the Gaussian shaped optical heating profile. (d) The attempted reconstruction of the 2D slice when 4 transducers (directly above the circular artifacts) record the data from the region. (e) The reconstruction of the sub-region when 256 transducers are used.

features. The classification method outlined is able to adapt to many different types of input signals. It simply requires a training set to learn from, and detectable differences in the signal. Although the basic SVM mechanism is used to discriminate only between two categories, multiple classifiers can be combined and used to discriminate between multiple categories. There is indeed further room for improvement in the classifier. The SVM was permitted to search for a decision function for only a short time, so a stronger decision function could still have been found. Also, the chosen wavelets, the window size, the step size, chosen wavelet packet filter basis, and the training set could be improved upon to generate a more accurate classifier by further fine-tuning.

In vascular tissue models, fractal trees are able to approximate specific tissue types to a considerable degree of realism. However, this is only an approximation of actual vascular geometry. Healthy kidney tissue, in particular, obeys a highly regular fractal pattern that can be modeled closely.[3] It may be an oversimplification, however, to assume that the fractal pattern holds across all scales. Vessels in other tissue types also obey fractal laws, but may have a higher degree of randomness and less regular branching intervals; however, the space filling properties are indeed fractal.[8,9] Other types of tissue have branching patterns that have been characterized and may be simulated by the methods presented. For example, the morphological branching parameters of colon endothelial tissue, is characterized by Ref. 40. Colon endothelial tissue could be suitable for clinical photoacoustic probing as it is more accessible than kidney tissue. Since the penetration depth of photoacoustic imaging is limited, to access kidney tissue in-vivo may require an intra-venous photoacoustic probe,[5] although there still may be some difficulty imaging an entire kidney away from large vessels.

To test the simulations on a more realistic tissue geometry than fractal trees, 3D OCT datasets were used. As seen in Figure 5, a 2D parametric image can be created that uses the classifier. Although only two datasets for 3D geometry were available, the classifier performs well to discriminate between them as shown. It should be noted that even though the tissue can be discriminated using the RF data with our algorithm, there is insufficient information to resolve the micro-vascular structures with the same data as shown in Figure 6d.

Instead of using models of OCT data, acquired data from photoacousitc microscopy could have been used. In this case, the dataset would have not been called a model, but rather, experimentally obtained in-vivo measurements. The OCT datasets were chosen due to their availability and because of their high image contrast and resolution. By using simulated signals, as in our approach, the effects related to vessel geometry are isolated from other tissue effects; hence, the analysis is on the structural morphology of the issue, and not on functional parameters such as blood volume and oxygen saturation.

Computationally, it is seen from Eqn. (10), that the windowing does not need to be done until after the WPD is performed. This is advantageous because it allows the filter tree structure of Figure 3 to be used once per RF-line and not once per feature vector. In addition, the approach uses a sliding window on the envelope of the DTCWPD[36] signals, which may be a new approach to feature vector generation. Ideally, the methods developed in this work would be applicable to detecting cancers via micro-vascular structures in skin or endothelial tissue which are accessible; or for analysing signals of larger vessels and larger tumors deep within tissue that cannot be fully resolved using a handheld transducer array.

It is likely that photoacoustic signals from in-vivo tissue will have features that allow them to be even more distinguishable than the current classifier, by combining the approach with functional imaging where blood oxygenation is measured.

8. CONCLUSIONS

In this work, a method was put forward for the classification of photoacoustic signals. It has been shown that the method has the potential to distinguish between different classes of detectable signals. Based on simulations, the method is able to detect the differences between normal and abnormal vasculature by its structural morphology. The classifier performs well even when the individual vessels of the tissue cannot be resolved.

The performance of the classifier has been characterized in the presence of noise using RF data. With a SNR of +30dB the classifier performs with a sensitivity of 96.4%, a selectivity of 78.6% and a p-value of 0.0000%. With a SNR of +10dB the classifier performs with a sensitivity of 60.7%, a selectivity of 89.2% and a p-value of 0.0007%. However, when the SNR is only +3dB the classifier performance is greatly reduced with a sensitivity of 100%, a selectivity of 0% and a p-value of 10.4%. A p-value of less than 5% indicates that there is a statistical significance whereby the null-hypothesis can be rejected.

The classifier is able to learn from a set of example signals what the difference between classes are. It is thereby able to adapt to different situations for other tissue classification problems.

Based on the analysis performed in this work, it does appear that the structural morphology plays a role in the detectable features of the photoacoustic signal. It is hopeful the signal differences related to structural morphology can be combined with existing methods for functional classification (such as blood oxygenation and blood volume) to produce even stronger methods for detection of vascular abnormality.

In addition, a method for simulating photoacoustic signals from large scale vascular tissue models has also been put forward, where vascular morphology was modelled as a fractal with cylindrical vessel segments. The simulator was validated against a FEM models on simple geometries.

The contributions in this work include studying the effect of the structural morphology of vasculature on photoacoustic RF signals; developing a method for photoacoustic simulation and modelling of large scale vascular structures in tissue that is more efficient than using a rasterized model; developing a classification algorithm based on the wavelet packet transform and support vector machines for classifying photoacoustic RF signals; and showing that it is possible to classify vascular tissue based on structural morphology using photoacoustic methods without resolving vascular structures.

Our future research endeavours include testing the classifier on clinically acquired photoacoustic data; further optimizing the SVM classifier with a larger training set; and incorporating inhomogeneous and more realistic tissue models into the simulation.

ACKNOWLEDGMENTS

Special thanks Ryerson Opto-acoustics Group for all of their help and support. Funding for this research has been provided by The National Sciences and Engineering Research Council of Canada (NSERC); The Canadian Institutes of Health Research (CIHR); The Canada Research Chairs Program (CRCP); and Ryerson University.

REFERENCES

[1] Jain, R. K., "Taming Vessels to Treat Cancer," *Scientific American* **1**, 56–63 (2008).

[2] Karshafian, R., *Modelling the structure of the tumour vasculature and its effect on Doppler ultrasound signals*, master's thesis, University of Toronto (2001).

[3] Zamir, M., "Arterial branching within the confines of fractal L-system formalism," *Gen. Physiol.* **118**(3), 267–275 (2001).

[4] Vaithilingam, S., Wygant, I. O., Sifferman, S., Zhuang, X., Furukawa, Y., Oralkan, O., Keren, S., Gambhir, S. S., and Khuri-Yakub, B. T., "Tomographic Photoacoustic Imaging Using Capacitive Micromachined Ultrasonic Transducer (CMUT) Technology," in [*IEEE Ultrasonics Symposium*], 397–400 (2006).

[5] Emelianov, S., Wang, B., Su, J., Karpiouk, A., Yantsen, E., Sokolov, K., Amirian, J., Smalling, R., and Sethuraman, S., "Intravascular Ultrasound and Photoacoustic Imaging," in [*30th Annual International IEEE EMBS Conference*], 2–5 (2008).

[6] Zhang, E., Laufer, J., and Beard, P., "Backward-mode multiwavelength photoacoustic scanner using a planar FabryPerot polymer film ultrasound sensor for high-resolution three-dimensional imaging of biological tissues," *Applied Optics* **47**(4), 561–577 (2008).

[7] Ermilov, S., Stein, A., Conjusteau, A., Gharieb, R., Lacewell, R., Miller, T., Thompson, S., Otto, P., Mccorvey, B., Khamapirad, T., Leonard, M., Oraevsky, A., Instruments, S. M., and Antonio, S., "Detection and noninvasive diagnostics of breast cancer with two-color laser optoacoustic imaging system," *Proc SPIE* **6437** (2007).

[8] Baish, J. W. and Jain, R. K., "Fractals and Cancer," *Cancer Research* **60**(7), 3683–3688 (2000).

[9] Grizzi, F., Russo, C., Colombo, P., Franceschini, B., Frezza, E. E., Cobos, E., and Chiriva-internati, M., "Quantitative evaluation and modeling of two-dimensional neovascular network complexity: the surface fractal dimension," *BMC Cancer* **9** (2005).

[10] Tafti, P. D., Van De Ville, D., and Unser, M., "Innovation Modelling and Wavelet Analysis of Fractal Processes in Bio-imaging," in [*ISBI*], 1501–1504 (2008).

[11] Cox, B. T. and Beard, P. C., "Fast calculation of pulsed photoacoustic fields in fluids using k-space methods," *J. Acoust. Soc. Am* **117**(6), 3616–3627 (2005).

[12] Rui, M., Bost, W., Weiss, E. C., Lemor, R., and Kolios, M. C., "Photoacoustic Microscopy and Spectroscopy of Individual Red Blood Cells," in [*OSA - Optics & Photonics Congress: BIOMED/DH 2010*], 3–5 (2010).

[13] Zhang, H. F., Maslov, K., Sivaramakrishnan, M., Stoica, G., and Wang, L. V., "Imaging of hemoglobin oxygen saturation variations in single vessels in vivo using photoacoustic microscopy," *Applied Physics Letters* **90** (2007).
[14] Wang, L. V., "Prospects of photoacoustic tomography," *Medical Physics* **35**(12), 5758–5767 (2008).
[15] Oraevsky, A. A. and Karabutov, A. A., [*Optoacoustic Tomography*], ch. 34, CRC Press, Boca Raton, Fla. (2003).
[16] Cobbold, R. S. C., [*Foundations of Biomedical Ultrasound*], Oxford University Press (2006).
[17] Bullitt, E., Muller, K., Jung, I., Lin, W., and Aylward, S., "Analyzing Attributes of Vessel Populations," *Med Image Anal* **9**(1), 39–49 (2005).
[18] Jain, R. K., "Normalization of Tumor Vasculature : An Emerging Concept in Antiangiogenic Therapy," *Science* **307**(58), 58–62 (2005).
[19] Yancopoulos, G. D., Davis, S., Gale, N. W., Rudge, J. S., Wiegand, S. J., and Holash, J., "Vascular-specific growth factors and blood vessel formation," *Nature* **407**(9), 242–248 (2000).
[20] Papetti, M. and Herman, I. M., "Mechanisms of normal and tumor-derived angiogenesis," *Americal Journal of Cell Physiology* **282**, 947–970 (2002).
[21] Carmeliet, P., "Angiogenesis in life, disease and medicine," *Nature* **438**(12), 932–936 (2005).
[22] Aylward, S. R. and Bullitt, E., "Initialization, noise, singularities, and scale in height ridge traversal for tubular object centerline extraction," *IEEE Trans. Med. Imag* **21**(2), 61–75 (2002).
[23] Herrero, M. A., Kohn, A., and Peres-Pomares, J. M., "Modelling Vascular Morphogenesis: Current Views on Blood Vessels Development," *Mathematical Models and Methods in Applied Sciences* **19**, 1483–1537 (2009).
[24] Kretowski, M., Rolland, Y., Bézy-wendling, J., and Coatrieux, J.-l., "Physiologically Based Modeling of 3-D Vascular Networks and CT Scan Angiography," *IEEE Transactions on Medical Imaging* **22**(2), 248–257 (2003).
[25] Kurz, H. and Godde, R., "Structural and Biophysical Simulation of Angiogenesis and Vascular Remodeling," *Developmental Dynamics* **220**(2), 387– 401 (2001).
[26] Merks, R. M. H. and Glazier, J. A., "Dynamic mechanisms of blood vessel growth," *Non-linearity* **19**, C0–C10 (2006).
[27] Meinhardt, H., "Morphogenesis of Lines and Nets," *Differentiation* **6**, 117–123 (1976).
[28] Wang, L., Bhalerao, A., and Wilson, R., "Analysis of Retinal Vasculature Using a Multiresolution Hermite Model," *IEEE Trans Medical Imaging* **26**(2), 137–152 (2007).
[29] Noble, J. A., "Ultrasound image segmentation and tissue characterization," *Proc IMechE, Part H: J. Engineering in Medicine* **224**(2), 307–316 (2010).
[30] Dydenko, I., Friboulet, D., Gorce, J., D, J., Bijnens, B., and Magnin, I. E., "Towards ultrasound cardiac image segmentation based on the radiofrequency signal," *Medical Image Analysis* **7**, 353–367 (2003).
[31] Joachims, T., Finley, T., and Yu, C. J., "Cutting-Plane Training of Structural SVMs," *Machine Learning* **77**(1), 27–59 (2009).
[32] Coifman, R. R. and Wickerhauser, M. V., "Entropy-based algorithms for best basis selection," *IEEE Transactions on Information Theory* **38**(2), 713–718 (1992).
[33] Unser, M., "Texture Classification and Segmentation Using Wavelet Frames," *IEEE Trans Image Processing* **4**(11), 1549–1560 (1995).
[34] Learned, R. and Willsky, A., "A Wavelet Packet Approach to Transient Signal Classification," *Applied and Computational Harmonic Analysis* **2**, 265–278 (1995).
[35] Taswell, C., "Near-best basis selection algorithms with non-additive information cost functions," in [*Proc. IEEE-SP TFTSA*], (1994).
[36] Bayram, I. and Selesnick, I. W., "On the Dual-Tree Complex Wavelet Packet," *IEEE Trans Signal Processing* **56**(6), 2298–2310 (2008).
[37] Zalev, J., *Detection and Monitoring for Cancer and Abnormal Vasculature by Photoacoustic Signal Characterization of Structural Morphology*, master's thesis, Ryerson University (2010).
[38] Mariampillai, A., Standish, B. A., Moriyama, E. H., Khurana, M., Munce, N. R., Leung, M. K. K., Jiang, J., Cable, A., Wilson, B. C., Vitkin, I. A., and Yang, V. X. D., "Speckle variance detection of microvasculature using swept-source optical coherence tomography," *Optics Letters* **33**(13), 1530–1532 (2008).
[39] Welch, B. L., "The generalization of 'student's' problem when several different population variances are involved," *Order A Journal On The Theory Of Ordered Sets And Its Applications* **34**(2), 28–35 (1947).
[40] Konerding, M. A., Fait, E., and Gaumann, A., "3D microvascular architecture of pre-cancerous lesions and invasive carcinomas of the colon," *British Journal of Cancer* **84**(2), 1354–1362 (2001).